

PathFinder: Advancing Path Loss Prediction for Single-to-Multi-Transmitter Scenario

Zhijie Zhong, Zhiwen Yu*, Senior Member, IEEE, Pengyu Li, Jianming Lv Member IEEE,
C. L. Philip Chen, Fellow, IEEE, Min Chen Fellow, IEEE

Abstract—Radio path loss prediction (RPP) is critical for optimizing 5G networks and enabling IoT, smart city, and similar applications. However, current deep learning-based RPP methods lack proactive environmental modeling, struggle with realistic multi-transmitter scenarios, and generalize poorly under distribution shifts, particularly when training/testing environments differ in building density or transmitter configurations. This paper identifies three key issues: (1) passive environmental modeling that overlooks transmitters and key environmental features; (2) overemphasis on single-transmitter scenarios despite real-world multi-transmitter prevalence; (3) excessive focus on in-distribution performance while neglecting distribution shift challenges. To address these, we propose PathFinder, a novel architecture that actively models buildings and transmitters via disentangled feature encoding and integrates Mask-Guided Low-rank Attention to independently focus on receiver and building regions. We also introduce a Transmitter-Oriented Mixup strategy for robust training and a new benchmark, single-to-multi-transmitter RPP (S2MT-RPP), tailored to evaluate extrapolation performance (multi-transmitter testing after single-transmitter training). Experimental results show PathFinder outperforms state-of-the-art methods significantly, especially in challenging multi-transmitter scenarios. Our code and project site are publicly available¹.

Index Terms—Wireless Communication, Radio Path Loss Prediction, Distribution Shift, Multi-Transmitter, 5G Communication

I. INTRODUCTION

The rapid advancement of 5G communication highlights benefits like low latency and extensive coverage, establishing a fundamental infrastructure for applications in the Internet of Things, intelligent driving, and smart cities [1, 2, 3, 4]. Among these, radio path loss prediction is crucial in communication network planning, signal forecasting, and drone base station/transmitter deployment. In essence, the Radio Path loss Prediction (RPP) task aims to predict the information loss distribution across regions based on the base station location and relevant data within a specific building environment [5, 6, 7, 8]. This is shown in Fig. 1(a).

Zhijie Zhong is with the School of Future Technology, South China University of Technology, Guangzhou, 510650, China, and also with the Pengcheng Laboratory, Shenzhen, 518066, China.

Zhiwen Yu is with the School of Computer Science and Engineering, South China University of Technology, Guangzhou, 510650, China, and also with the Pengcheng Laboratory, Shenzhen, 518066, China. Email: zhwyu@scut.edu.cn. Telephone number: 86-20-62893506. Fax number: 86-20-39380288.

Pengyu Li, Jianming Lv, C. L. Philip Chen and Min Chen are with the School of Computer Science and Engineering, South China University of Technology, Guangzhou, 510650, China.

*Corresponding author: Zhiwen Yu.

¹<https://emorzz1g.github.io/PathFinder/>

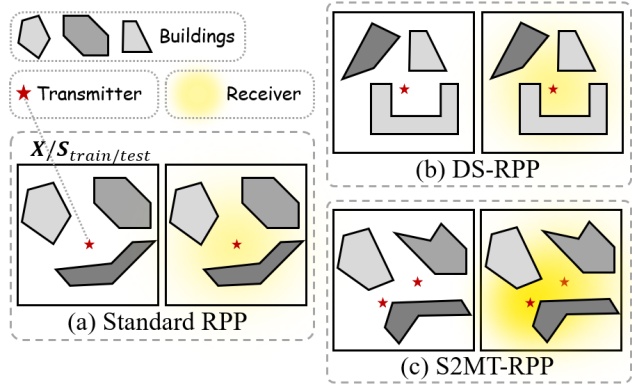


Fig. 1: Examples of the three types of RPP tasks.

Challenges in this predictive task often arise from the height and density of buildings in different settings. Additionally, the prediction is complicated by intricate physical phenomena such as diffraction, refraction, and reflection affecting radio signal propagation [9, 10, 5].

The ray tracing method is widely used for predicting radio path loss in mobile communication environments [11, 9]. While this method provides accurate predictions, its intricate modeling and computational processes make it unsuitable for real-time applications [9, 12]. Therefore, it is better suited for design tasks like base station site selection that do not require immediate results. Radio path loss prediction essentially involves estimating or generating predictions. The increasing need for real-time radio path loss predictions, combined with advancements in deep learning, has sparked significant interest in integrating deep learning methods into this area [13, 11, 9]. Deep learning-based predictive models [14, 15, 16] utilize end-to-end learning to reveal implicit relationships between building structures and electromagnetic propagation, resulting in faster and more adaptable model performance for various scenarios. Initially, convolutional neural networks were successfully applied to this task [13]; however, the lack of extensive validation on real-world datasets was a limitation at the outset, mainly due to the deficiencies in publicly available datasets. Addressing this, Levie et al. [9] were the first to tackle the dataset scarcity by introducing the first 2D radio point path loss prediction task and dataset, RadioMapSeer, along with the RadioUNet model for predicting radio path loss. RadioMapSeer, a dataset simulated on a real map using ray tracing software, did not consider building height information or diverse transmitter locations due to algorithm constraints at

the time. Recognizing this limitation, subsequent researchers Yapar et al. [11] developed a new dataset, RadioMapSeer3D, expanding on the RadioMapSeer methodology by incorporating building height information and offering a wider range of transmitter locations. Over time, this dataset has become the primary public dataset in the field [17, 18]. The development of datasets has led to the emergence of numerous deep learning models [18, 17, 19] for radio path loss prediction, as detailed in the related work section. However, current radio path loss prediction models mainly concentrate on enhancing model performance and refining prediction accuracy, overlooking other crucial aspects of the task. We have pinpointed three vital issues that have been underexplored in previous studies but substantially impede the practical utility of RPP models.

Problem 1: Current models demonstrate insufficient proactive modeling of the environment. Previous studies [9, 20, 10, 18] consider the transmitter as an inherent, static feature on the map. This passive modeling strategy causes the models to disregard the significance of actively incorporating the transmitter, resulting in inadequate learning of the propagation relationship between the transmitter and receiver. Additionally, existing research overlooks the independent guidance of the model's focus on building regions and receivers, neglecting their essential roles within the environment.

Problem 2: A substantial gap exists between modeling single-transmitter scenarios and addressing real-world multi-transmitter environments. Previous studies [9, 20, 10, 18] have predominantly focused on single-transmitter scenarios (e.g., Fig. 1(b)), while neglecting the prevalence of multiple transmitters in practical settings. However, in real-world 5G deployments, the “single-to-multi-transmitter (S2MT)” shift is widespread. For instance, base stations are dynamically added in expanding urban areas. Despite this, existing models lack the ability to extrapolate from single-transmitter training data to multi-transmitter testing scenarios. For example, models trained on data with 1 transmitter often exhibit notable drops in accuracy when tested on scenes with 2–4 transmitters (Fig. 1(c)). This limitation in extrapolation directly restricts the practical utility of current RPP models, rendering it a critical issue that demands resolution.

In order to address the two major issues identified in previous research, we contribute in three aspects:

- 1) To remedy the deficiency in the proactive modeling capabilities of models concerning the environment and address problem 1, we propose PathFinder, which utilizes decoupled features to actively model both buildings and transmitters, thereby enhancing the model's attentiveness to these components. Furthermore, Mask-Guided Low-rank Attention is introduced to help the model focus independently on receiver and building regions.
- 2) To address problem 2, we introduce Transmitter-Oriented Mixup for model training. Based on this approach, we propose a new evaluation benchmark called single-to-multi-transmitter radio path loss prediction (S2MT-RPP). This benchmark enables a more comprehensive assessment of the capabilities of various models.
- 3) We conduct a comparative analysis between the proposed PathFinder and the current state-of-the-art (SOTA)

methods, empirically demonstrating that our approach surpasses the performance of existing SOTA techniques.

II. RELATED WORK

A. Radio Pathloss Prediction

Early deep learning RPP models, limited by dataset scale, saw Teganya and Romero [13] construct a convolutional autoencoder (AE) to learn intrinsic data structures through dimensionality reduction [21]. However, limited parameters restricted the model's expressive capacity, making it suitable only for small scale data scenarios [22, 23]. Following the RadioMapSeer dataset release, RadioUNet [9] first applied UNet to 2D radio path loss prediction, using two independent UNet sub models to learn features from building and transmitter channels. Similarly, DeepREM [14] used a UNet and conditional generative adversarial network (CGAN) model to estimate RPP from sparse measurements, eliminating the need for additional geographic information. However, this method relies on real radio path loss maps as conditional inputs, limiting its generalization. Additionally, RadioDIP [20] predicted path loss in radio signal maps by combining a pre trained RadioUNet with deep image priors (DIP). Nonetheless, this approach did not explore building height's influence on path loss. With increased demand for prediction accuracy, RadioDiff [10] constructed a diffusion model using attention mechanisms and adaptive fast Fourier transforms, significantly enhancing RPP detail representation. However, diffusion models' inherent multi step sampling led to prolonged inference times and increased memory consumption, limiting real time applicability. Moreover, slow inference prevented considering building height information. Recently, PMNet [18] emerged as the state of the art RPP algorithm, introducing a pyramid structure for multi scale feature extraction and applying dilated convolutions to expand the receptive field. Similarly, REMNet [17] achieved precise RPP construction by enlarging the receptive field and mitigating information loss, using multiple sets of dilated convolutions with varying kernel sizes to learn different scale features concurrently. However, these approaches have not incorporated additional information to proactively guide building region modeling, treating them merely as another data processing channel within images.

B. Distribution Shift in Radio Path Loss Prediction

Machine learning algorithms typically assume training and testing data come from the same distribution. However, real world models often encounter new data that deviates from the training distribution, known as distribution shift. Models trained on a specific distribution may struggle with distribution shift data due to differing features and attributes.

In wireless communication, intricate and variable environments like diverse geographical features, building layouts, and weather conditions cause varying signal propagation. An RPP model trained in one urban area may perform poorly in another city with different terrain or architecture. This typical RPP distribution shift arises from inconsistent environmental or scenario factors between training and testing.

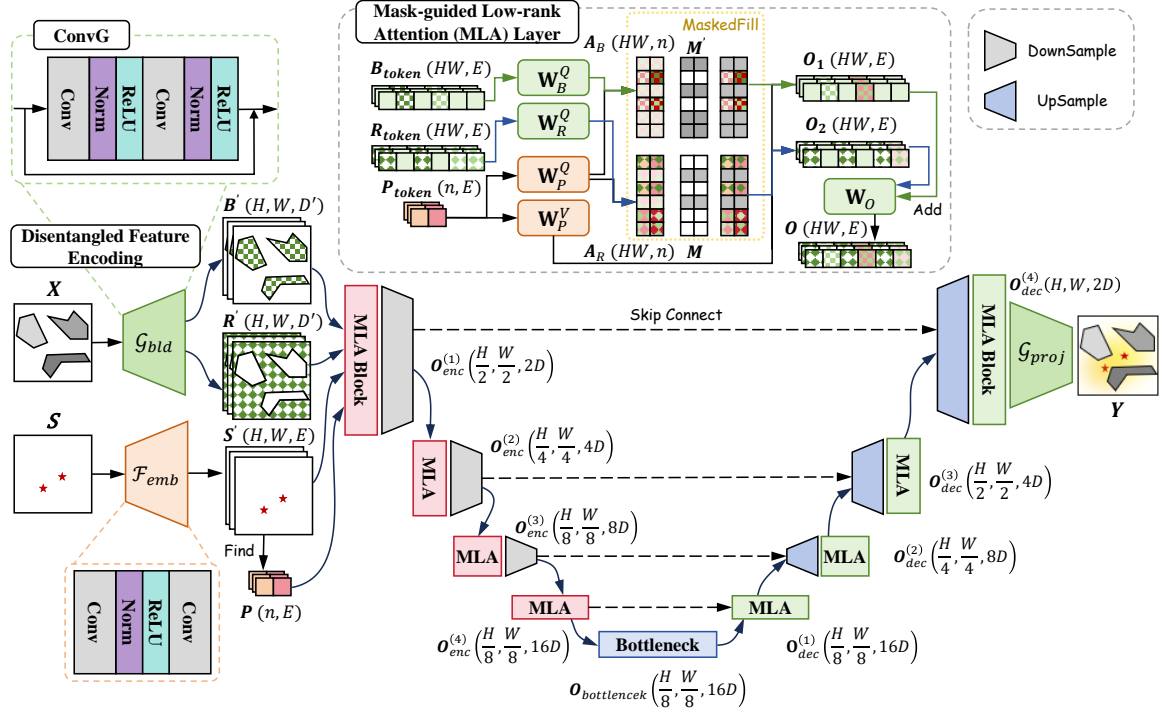


Fig. 2: The framework diagram and workflow of PathFinder.

Research on RPP under distribution shift is nascent. Yapar et al. [24] explored RPP across building regions with distribution shifts, using different architectural maps for training and testing (i.e., differing building layout distributions). Mitchell et al. [25] identified another shift: deploying RPP in a region often requires extensive, costly, and challenging sampling. They proposed training models with a subset of RPP samples, as obtaining full samples can be unfeasible. This creates a 'sample availability induced distribution shift' between limited training data and full scene testing.

This study introduces a novel single to multi transmitter distribution shift: models learn from single transmitter RPP maps but must predict cumulative path loss from multiple transmitters during deployment. The core shift lies in the number of transmitters, a key signal propagation factor, between training and testing. To address this, we propose a dataset independent, reusable distribution shift evaluation task: Single to Multi Transmitter Radio Path Loss Prediction (S2MT RPP). This fills a gap in dedicated benchmarks for transmitter related RPP distribution shifts.

III. PRELIMINARIES

A. Problem Definition

Real world propagation involves diffraction, refraction, and reflection. Building materials cause variations in their inherent coefficients. Ray tracing is often too slow for real time radio path loss prediction [11].

Following previous works [18, 17, 11], we model actual $PL(d)$ as a prediction problem. Given an environmental map $\mathbf{X} \in \mathbb{R}^{H \times W}$ with height H and width W in meters, $\mathbf{X}_{x,y}$ represents the normalized building height, ranging from 0 to 1.

The transmitter is a point (T_x, T_y) in the environmental map, translated into an image representation $\mathbf{S} \in \mathbb{R}^{H \times W}$. Here, $\mathbf{S}_{T_x, T_y} = I$, where I is the transmitter's height. Model f learns the relationship between \mathbf{X} and \mathbf{S} to predict the final radio path loss map $\mathbf{Y} \in \mathbb{R}^{H \times W}$, expressed as: $\mathbf{Y} = f(\mathbf{X}, \mathbf{S}; \theta)$, where θ represents the optimizable parameters of model f .

B. Distribution Shift RPP

In this subsection, we formally define distribution shift radio path loss prediction (DS-RPP) and single-to-multi-transmitter distribution shift radio path loss prediction (MT-RPP), consistent with the distribution shift terminology used in previous sections.

For DS-RPP, we define it as the path loss prediction problem where there is a discrepancy in data distribution between the training and testing phases (the core characteristic of distribution shift). Specifically, during the training phase, the model learns the mapping between the environmental map $\mathbf{X}_{\text{train}} \in \mathbb{R}^{H \times W}$ and the transmitter location map $\mathbf{S}_{\text{train}} \in \mathbb{R}^{H \times W}$ based on the training data distribution $\mathcal{D}_{\text{train}} = \{\mathbf{X}_{\text{train}}, \mathbf{S}_{\text{train}}, \mathbf{Y}_{\text{train}}\}$ to predict the path loss map $\mathbf{Y}_{\text{train}} \in \mathbb{R}^{H \times W}$. The mathematical expression for this process is: $\mathbf{Y}_{\text{train}} = f(\mathbf{X}_{\text{train}}, \mathbf{S}_{\text{train}}; \theta)$, where $f(\cdot; \theta)$ denotes the model, and θ represents the model parameters.

In the testing phase, the model encounters data from a different distribution $\mathcal{D}_{\text{test}} = \{\mathbf{X}_{\text{test}}, \mathbf{S}_{\text{test}}, \mathbf{Y}_{\text{test}}\}$ and must predict the path loss map $\mathbf{Y}_{\text{test}} \in \mathbb{R}^{H \times W}$ based on the testing environmental map $\mathbf{X}_{\text{test}} \in \mathbb{R}^{H \times W}$ and the testing transmitter location map $\mathbf{S}_{\text{test}} \in \mathbb{R}^{H \times W}$: $\mathbf{Y}_{\text{test}} = f(\mathbf{X}_{\text{test}}, \mathbf{S}_{\text{test}}; \theta)$. Here, $\mathcal{D}_{\text{train}} \neq \mathcal{D}_{\text{test}}$ embodies the core characteristic of distribution shift scenarios.

Furthermore, we define S2MT-RPP as the distribution shift path loss prediction problem in multi-transmitter scenarios. Its mathematical expression is:

$$\mathbf{Y}_{\text{test}} = f \left(\mathbf{X}_{\text{test}}, \left\{ \mathbf{S}_{\text{test}}^{(1)}, \mathbf{S}_{\text{test}}^{(2)}, \dots, \mathbf{S}_{\text{test}}^{(N)} \right\}; \theta \right), \quad (1)$$

where $\left\{ \mathbf{S}_{\text{test}}^{(1)}, \mathbf{S}_{\text{test}}^{(2)}, \dots, \mathbf{S}_{\text{test}}^{(N)} \right\}$ represents the location maps of N transmitters ($N \geq 2$), and the key distribution shift lies in the *number of transmitters* (single in $\mathcal{D}_{\text{train}}$, multiple in $\mathcal{D}_{\text{test}}$).

IV. PATHFINDER MODEL

PathFinder consists of three main components: Disentangled Feature Encoding, Transmitter-Aware Prompt, and Mask-Guided Low-rank Attention. Fig. 2 illustrates its architecture and workflow. The environment map \mathbf{X} and transmitter \mathbf{S} are first processed by Disentangled Feature Encoding (DFE), producing decoupled building features \mathbf{B}' , transmitter features \mathbf{S}' , and a Transmitter-Aware Prompt \mathbf{P} derived from \mathbf{S}' . At its core, PathFinder employs a UNet-based learning network. The encoder includes Mask-Guided Low-rank Attention (MLA) Blocks and downsample blocks, while the decoder features MLA Blocks and upsample blocks. The bottleneck contains two convolutional layers. In the encoder, each MLA Block (except the last) is followed by a downsample block to halve the feature map size. Similarly, in the decoder, each MLA Block (except the first) is followed by an upsample block to double the feature map size and adjust channel numbers. Finally, the path loss prediction head uses the decoder's final feature maps to estimate path loss.

A. Disentangled Feature Encoding

During model training, the transmitter's position varies, while building positions remain fixed. Previous methods overlooked this distinction, leading to redundant feature learning [17, 18]. To resolve this, we propose Disentangled Feature Encoding (DFE), which separates building and transmitter feature learning, simplifying feature extraction.

Building maps are represented as a single channel $\mathbf{B} \in \mathbb{R}^{H \times W}$, and transmitter information as $\mathbf{S} \in \mathbb{R}^{H \times W}$. However, this representation retains redundant transmitter features, complicating dynamic learning. To address this, we introduce a Transmitter-Aware Prompt (Tx-Prompt) method, transforming multiple \mathbf{S} data into dynamic prompt vectors.

We first extract transmitter details from \mathbf{S} , where a single transmitter is $\mathbf{s} = (i, j, I)$, with i, j indicating position and I the height. Using convolutional feature extraction $f_{\text{emb}}(\cdot)$, \mathbf{S} is mapped to high-dimensional features: $f_{\text{emb}} : \mathbf{S} \in \mathbb{R}^{H \times W} \rightarrow \mathbf{S}' \in \mathbb{R}^{H \times W \times E}$, where E is the embedding dimension. The mapping is defined as: $\mathcal{F}_{\text{emb}}(\mathbf{S}) = (\text{Conv} \circ \text{BN} \circ \text{ReLU} \circ \text{Conv})(\mathbf{S})$, where $\text{Conv}(\cdot)$ represents 2D convolution, $\text{BN}(\cdot)$ is batch normalization, and $\text{ReLU}(\cdot)$ is the activation function.

For n transmitters $\mathbb{S} = \{s_1, s_2, \dots, s_n\}$, their prompt vectors $\mathbf{P} = \{p_1, p_2, \dots, p_n\}$ are retrieved as $\mathbf{P} = \{\text{find}(\mathbf{S}', i, j)\}^n$, where find indexes the corresponding vector in \mathbf{S}' . Thus, $\mathbf{P} \in \mathbb{R}^{n \times E}$ serves as the Tx-Prompt.

Building features are independently learned using a feature encoder g_{bld} , such that: $g_{\text{bld}} : \mathbf{B} \in \mathbb{R}^{H \times W} \rightarrow \mathbf{B}' \in \mathbb{R}^{H \times W \times D'}$, where $D' = E$. To capture diverse building features, we employ a convolution module ConvG with residual connections and group normalization:

$$\begin{aligned} \mathbf{B}' &= g_{\text{bld}}(\mathbf{B}) = \text{ConvG}(\mathbf{B}) + \mathbf{B}, \\ \text{ConvG}(\mathbf{B}) &= (\text{ReLU} \circ \text{GN} \circ \text{Conv} \circ \text{ReLU} \circ \text{GN} \circ \text{Conv})(\mathbf{B}). \end{aligned} \quad (2)$$

Here, $\text{GN}(\cdot)$ denotes group normalization.

Ultimately, DFE enables decoupled learning for buildings and transmitters, producing \mathbf{B}' and \mathbf{S}' , along with the transmitter prompt feature \mathbf{P} .

B. Mask-Guided Low-rank Attention

To predict high-frequency information in path loss, we continue with the UNet architecture established in previous works. Specifically, the UNet consists of an encoder, a decoder, and a bottleneck, with both the encoder and decoder comprising $L (= 4)$ Mask-Guided Low-rank Attention Blocks (MLA Blocks), as illustrated in Fig. 2. Each block consists of two ConvG layers and one Mask-Guided Low-rank Attention Layer (MLA Layer). In the feature encoding phase, after each block, a convolutional network is applied to double the channel count of the data while halving the spatial dimensions of the feature maps compared to the previous layer. In the feature decoding phase, the input to the j -th MLA Block is derived from the output of the $(L - j + 1)$ -th layer in the encoder and the output of the $(j - 1)$ -th MLA Block. The input to the first MLA Block of the decoder consists of the output from the last layer of the encoder and the output from the bottleneck. To succinctly describe the workflow of the Mask-Guided Low-rank Attention Block within each layer, it is important to note that the feature map dimensions D differ across layers. At the first of each layer, the feature map dimension transitions to $D^* = 2D$, indicating the dimension of the feature map for the subsequent layer, via Eq. (3). For a better intuitive understanding of the variant in dimension, refer to Fig. 2.

To enable PathFinder to learn the global information of the environmental region, we combine the features \mathbf{B}' and \mathbf{S}' , resulting in $\mathbf{Z} = \mathbf{X}'(\mathbf{B}' + \mathbf{R}') + \mathbf{S}'$ as the input to each ConvG. Thus, the input to the MLA Layer can be expressed as:

$$\mathbf{X}_1 = (\text{ConvG} \circ \text{ConvG})(\mathbf{Z}), (\mathbb{R}^{H \times W \times D'} \rightarrow \mathbb{R}^{H \times W \times D}). \quad (3)$$

Here, D' and D denote the dimensions of the current layer and the previous layer. For the first layer, D' is the original dimension of building features. However, this approach alone does not explicitly guide the model in learning how to predict radio path loss, as it does not provide clear guidance on the relationships between the transmitter and the buildings, as well as between the transmitter and the receiver.

To further address this issue, we consider the environmental map \mathbf{X}_1 as comprising two components: the building region \mathbf{B}' and the non-building region, which corresponds to the receiver region \mathbf{R}' . By utilizing a mask to guide the model in

independently computing attention scores, we introduce Mask-Guided Low-rank Attention to explicitly learn the global relationships between the building region \mathbf{B}' and the transmitter prompts \mathbf{P} , as well as between the receiver region \mathbf{R}' and the transmitter prompts \mathbf{P} . Unlike traditional self-attention mechanisms, this method allows for more efficient and rapid optimization. The segmentation of the original environmental map significantly reduces the sequence length of the attention, while the Tx-Prompt-guided approach further lowers the computational complexity of cross-attention. Additionally, to enable the model to capture key low-rank information and enhance computational efficiency, we first perform a low-rank transformation \mathcal{F}_{LR} on the environmental map \mathbf{X}_1 , expressed as:

$$\mathbf{X}_{LR} = \mathcal{F}_{LR}(\mathbf{X}_1) = (\text{Conv} \circ \text{BN})(\mathbf{X}_1). \quad (4)$$

Before constructing the MLA, we unify different features into sequence tokens using reshape and Layer Norm (LN(..)) [26, 27]. The building region feature \mathbf{B}' , the receiver region feature \mathbf{R}' , and the Tx-Prompt \mathbf{P} are converted into building sequence tokens, receiver sequence tokens, and Tx-Prompt tokens, respectively:

$$\mathbf{B}_{token} = (\text{LN} \circ \text{Reshape} \circ \mathcal{F}_{LR})(\mathbf{X}_1), \quad (\mathbb{R}^{H \times W \times D} \rightarrow \mathbb{R}^{HW \times E}) \quad (5)$$

$$\mathbf{R}_{token} = (\text{LN} \circ \text{Reshape} \circ \mathcal{F}_{LR})(\mathbf{X}_1), \quad (\mathbb{R}^{H \times W \times D} \rightarrow \mathbb{R}^{HW \times E}) \quad (6)$$

$$\mathbf{P}_{token} = \text{LN}(\mathbf{P}), \quad (\mathbb{R}^{n \times E} \rightarrow \mathbb{R}^{n \times E}), \quad (7)$$

where E denotes a lower-dimensional space, specifically $E < D$.

Next, we define two sets of multi-head query matrices to query the relevant features of the building sequence tokens and the receiver sequence tokens. The parameters for the former's multi-head query matrix are denoted as \mathbf{W}_B^Q , while those for the latter are \mathbf{W}_R^Q . The queried features are represented as $\mathbf{Q}_B = \mathbf{B}_{token} \mathbf{W}_B^Q$ and $\mathbf{Q}_R = \mathbf{R}_{token} \mathbf{W}_R^Q$. Simultaneously, we define multi-head key and value matrices to represent the relevant features of the Tx-Prompt tokens, denoted as \mathbf{W}_{K_P} and \mathbf{W}_P^V . Thus, the key and value features for the Tx-Prompt tokens are represented as $\mathbf{K}_P = \mathbf{P}_{token} \mathbf{W}_P^K$ and $\mathbf{V}_P = \mathbf{P}_{token} \mathbf{W}_P^V$.

Subsequently, we compute the cross-attention [28] scores between the building sequence tokens and the Tx-Prompt tokens, as well as between the receiver sequence tokens and the Tx-Prompt tokens:

$$\mathbf{A}_B = \frac{\mathbf{Q}_B \mathbf{K}_P^\top}{\sqrt{E}}, \quad \mathbf{A}_R = \frac{\mathbf{Q}_R \mathbf{K}_P^\top}{\sqrt{E}}. \quad (8)$$

Assuming the guiding mask for the building region is $\mathbf{M} \in \{0, 1\}^{HW \times 1}$, the guiding mask for the receiver region is $\mathbf{M}' = \mathbf{I} - \mathbf{M}$, with both being complementary sets. We can then derive the final cross-attention scores related to the building sequence and receiver tokens:

$$\mathbf{A}_B = \text{Fill}(\mathbf{A}_B, \mathbf{M}') \in \mathbb{R}^{HW \times n}, \quad (9)$$

$$\mathbf{A}_R = \text{Fill}(\mathbf{A}_R, \mathbf{M}) \in \mathbb{R}^{HW \times n}. \quad (10)$$

Here, the Fill operation fills the cross-attention scores in the \mathbf{M}' region with negative infinity. Consequently, the retained cross-attention scores are solely related to the mask \mathbf{M} .

Finally, we utilize the cross-attention scores to identify the regions most closely associated with the value features of the building area and the transmitter prompts, as well as the regions of the receiver area that are most correlated with the value features of the transmitter prompts. The final results are then linearly aggregated. This process can be expressed as follows:

$$\mathbf{O}_1 = \text{Softmax}(\mathbf{A}_B) \mathbf{V}_P, \quad (\mathbb{R}^{HW \times n} \rightarrow \mathbb{R}^{HW \times E}) \quad (11)$$

$$\mathbf{O}_2 = \text{Softmax}(\mathbf{A}_R) \mathbf{V}_P, \quad (\mathbb{R}^{HW \times n} \rightarrow \mathbb{R}^{HW \times E}) \quad (12)$$

$$\mathbf{O} = \text{Conv} \left(\frac{\mathbf{O}_1 + \mathbf{O}_2}{2} \mathbf{W}_O \right), \quad (\mathbb{R}^{HW \times E} \rightarrow \mathbb{R}^{HW \times E}), \quad (13)$$

$$\mathbf{O} = \text{Reshape}(\mathbf{O}) \quad (\mathbb{R}^{HW \times E} \rightarrow \mathbb{R}^{H \times W \times D}), \quad (14)$$

where \mathbf{W}_O is the parameter matrix for linear aggregation. The operation Conv serves to restore the features from the low-rank space to the high-dimensional space, while the Reshape function converts the features from a token sequence into a feature map.

C. PathFinder Pipeline

Below is a detailed explanation of how the encoder, bottleneck, and decoder process feature maps, as shown in Fig. 2. In the encoder, except for the last layer, the output feature $\mathbf{O}_{enc}^{(j)}$ of the j -th layer undergoes downsampling: $\mathbf{O}_{enc}^{(j)} = \text{DownSample}(\mathbf{O}_{enc}^{(j)}), \quad (\mathbb{R}^{H \times W \times D} \rightarrow \mathbb{R}^{\frac{H}{2} \times \frac{W}{2} \times D})$. The bottleneck contains two ConvG layers, producing the feature: $\mathbf{O}_{bottleneck} = (\text{ConvG} \circ \text{ConvG})(\mathbf{O}^{(L)})$. In the decoder, the input to the j -th layer, $\mathbf{Z}^{(j)}$, is formed by concatenating the previous decoder output $\mathbf{O}_{dec}^{(j-1)}$ (or $\mathbf{O}_{bottleneck}$ for the first layer) with the corresponding encoder output $\mathbf{O}_{enc}^{(L-j+1)}$ along the channel dimension:

$$\mathbf{Z}^{(j)} = \begin{cases} [\mathbf{O}_{dec}^{(j-1)}, \mathbf{O}_{enc}^{(L-j+1)}], & j > 1, \\ [\mathbf{O}_{bottleneck}, \mathbf{O}_{enc}^{(L-j+1)}], & j = 1. \end{cases} \quad (15)$$

Except for the first layer, the output $\mathbf{O}_{dec}^{(j)}$ of each decoder layer is upsampled, doubling the feature map size: $\mathbf{O}_{dec}^{(j)} = \text{UpSample}(\mathbf{O}_{dec}^{(j)}), \quad (\mathbb{R}^{H \times W \times D} \rightarrow \mathbb{R}^{2H \times 2W \times D})$. Finally, the path loss prediction head \mathcal{G}_{pred} estimates the radio path loss: $\hat{\mathbf{Y}} = \mathcal{G}_{pred}(\mathbf{O}_{dec}^{(L)})$.

D. Transmitter-Oriented Mixup

In the field of computer vision, data augmentation methods [29, 30, 31] are typically designed to enhance the model's generalization capability by expanding the dataset [32]. In the context of path loss prediction, common techniques such as image rotation, horizontal, vertical, and diagonal flipping have been employed and proven effective. However, these methods represent generic strategies from the image processing domain and lack task-specific targeting, failing to further enhance the model's path loss prediction abilities. To overcome this limitation, we draw inspiration from Mixup [30] and propose

the Transmitter-Oriented Mixup (TOM) data augmentation, grounded in the principle of additivity in signal propagation [33, 34]. Additionally, we establish new complex scenario tests based on this strategy to evaluate the generalization capabilities of different models, with detailed descriptions provided in the experimental section.

To fully leverage the contributions of different transmitters and their generated path losses, let us assume the original environmental map is \mathbf{X} , which may contain a set of n transmitters $\mathbb{S} = \{s_1, s_2, \dots, s_n\}$. The corresponding radio path loss maps generated by these transmitters are denoted as $\mathbb{Y} = \{\mathbf{Y}_1, \mathbf{Y}_2, \dots, \mathbf{Y}_n\}, \mathbf{Y}_i \in \mathbb{R}^{H \times W}$. Given any two transmitters i and j along with their radio path loss maps \mathbf{Y}_i and \mathbf{Y}_j , according to the principle of additivity in signal propagation, if the weights of the transmitters are a and b , the resulting combined radio path loss map can be expressed as $\mathbf{Y} = a\mathbf{Y}_i + b\mathbf{Y}_j$. This implies that, under the same environmental map conditions, the mixed radio path loss map is solely related to the transmitters. Based on this principle, we propose the Transmitter-Oriented Mixup data augmentation.

Specifically, given any base image augmentation function f_{aug} (including image rotation, horizontal, vertical, and diagonal flipping, etc.), and sampling mix weights $\beta \sim \text{Beta}(\alpha, \alpha), \beta \in [0, 1]$, where β follows a Beta distribution with parameters both set to α , the mixed environmental map can be expressed as $\mathbf{X}_{mixup} = f_{aug}(\mathbf{X})$.

Given the set of transmitters \mathbb{S} , which can be transformed into transmitter maps $\{S_1, S_2, \dots, S_n\}, S_i \in \mathbb{R}^{H \times W}$, we randomly select two transmitter maps S_i and S_j . The final mixed transmitter map and radio path loss map are then given by:

$$\begin{aligned} S_{mixup} &= \beta f_{aug}(S_i) + (1 - \beta) f_{aug}(S_j), \\ \mathbf{Y}_{mixup} &= \beta f_{aug}(\mathbf{Y}_i) + (1 - \beta) f_{aug}(\mathbf{Y}_j). \end{aligned} \quad (16)$$

Finally, we utilize these mixed samples for model training to enhance the model's generalization capability.

E. Model Optimization

To ensure the accuracy of radio path loss map predictions, the mean squared error (MSE) loss [35, 36] is commonly employed to optimize the model. However, during the early stages of model training, when the model's output significantly deviates from the target, the gradients of the MSE can become excessively large, leading to instability in training. Moreover, due to the substantial number of parameters in the UNet architecture, the slow optimization speed in the initial phase is exacerbated by the MSE loss. To address these shortcomings, we propose the Momentum Prediction Loss (MPL). This loss function introduces an additional parameter δ for adaptive momentum updates, smoothing the weights of the MSE loss and the mean absolute error (MAE) loss. It can be expressed as follows:

$$\mathcal{L} = \begin{cases} \frac{(\mathbf{Y} - \hat{\mathbf{Y}})^2}{2}, & |\mathbf{Y} - \hat{\mathbf{Y}}| \leq \delta \\ \delta |\mathbf{Y} - \hat{\mathbf{Y}}| - \frac{\delta^2}{2}, & |\mathbf{Y} - \hat{\mathbf{Y}}| > \delta \end{cases} \quad (17)$$

where $\hat{\mathbf{Y}}$ represents the model's predicted radio path loss map.

After each iteration, the parameter δ is updated based on the average predicted MAE loss momentum from the current batch of data (e.g., N samples) as follows: $\delta = \max\{0.9 \cdot \delta, \frac{\sum_i^N |\mathbf{Y}_i - \hat{\mathbf{Y}}_i|}{N}\}$.

V. THEORETICAL ANALYSIS

A. Complexity Analysis of Mask-Guided Low-rank Attention

Standard self-attention mechanisms typically incur a quadratic computational complexity with respect to the input sequence length [37, 38]. Given a feature map with spatial dimensions $H \times W$, the sequence length is $N = HW$. The complexity of standard attention is $\mathcal{O}(N^2d)$, where d is the feature dimension. This is computationally prohibitive for high-resolution path loss maps.

In contrast, our proposed Mask-Guided Low-rank Attention (MLA) significantly reduces this cost. By disentangling the transmitter prompt \mathbf{P} from the environmental features, we utilize \mathbf{P} as the bridge for attention computation. Let n denote the number of transmitters (where $n \ll N$) and E be the embedding dimension. The computation of queries $\mathbf{Q}_B, \mathbf{Q}_R \in \mathbb{R}^{N \times E}$ and keys/values $\mathbf{K}_P, \mathbf{V}_P \in \mathbb{R}^{n \times E}$ involves linear projections with complexity $\mathcal{O}(NE^2 + nE^2)$.

The cross-attention score calculation, e.g., $\mathbf{A}_B = \mathbf{Q}_B \mathbf{K}_P^\top$, involves the multiplication of an $(N \times E)$ matrix by an $(E \times n)$ matrix, resulting in a complexity of $\mathcal{O}(NnE)$. Similarly, the aggregation step $\mathbf{O}_1 = \text{Softmax}(\mathbf{A}_B)\mathbf{V}_P$ incurs $\mathcal{O}(NnE)$. Since n is a small constant (representing the number of transmitter prompts) and E is the low-rank dimension, the total complexity of our MLA is:

$$\mathcal{C}_{MLA} = \mathcal{O}(NnE) \approx \mathcal{O}(N). \quad (18)$$

Thus, PathFinder achieves $\mathcal{O}(N)$ complexity with respect to the image resolution, ensuring scalability for large-scale urban environments compared to the $\mathcal{O}(N^2)$ complexity of traditional methods.

B. Theoretical Justification for S2MT Generalization

The core challenge of the S2MT-RPP task is extrapolating from a domain \mathcal{D}_{single} to \mathcal{D}_{multi} . We justify the effectiveness of our Transmitter-Oriented Mixup (TOM) based on the physical principle of signal superposition.

1) *Physical Superposition Consistency*: In electromagnetic theory, the received signal strength from multiple incoherent sources at a location \mathbf{r} approximates the sum of the powers from individual sources (in linear scale). Let $\Phi(\mathbf{X}, \mathbf{S})$ be the ideal physical propagation function. For a set of transmitters $\mathbb{S} = \{s_1, \dots, s_k\}$, the total path loss map satisfies the additivity property locally:

$$\Phi(\mathbf{X}, \sum_{i=1}^k S_i) \approx \sum_{i=1}^k \Phi(\mathbf{X}, S_i). \quad (19)$$

Standard training on single-transmitter data \mathcal{D}_{single} does not guarantee that the neural network f_θ satisfies Eq. (19).

2) *Linearity Inductive Bias via TOM*: Our Transmitter-Oriented Mixup strategy constructs synthetic training samples via convex combinations. By minimizing the loss on mixed samples:

$$\mathcal{L}_{mix} = \|f_\theta(\mathbf{X}, \beta\mathbf{S}_i + (1-\beta)\mathbf{S}_j) - (\beta\mathbf{Y}_i + (1-\beta)\mathbf{Y}_j)\|^2, \quad (20)$$

we explicitly regularize the model f_θ to behave linearly with respect to the transmitter input space \mathbf{S} . Let the linearization error be $\epsilon_{lin} = |f_\theta(\lambda\mathbf{S}_1 + \mu\mathbf{S}_2) - (\lambda f_\theta(\mathbf{S}_1) + \mu f_\theta(\mathbf{S}_2))|$. The TOM strategy minimizes the upper bound of ϵ_{lin} . Consequently, when testing on a multi-transmitter input $\mathbf{S}_{test} = \sum \mathbf{S}^{(i)}$, the model prediction approximates the sum of individual predictions:

$$f_\theta(\mathbf{X}, \mathbf{S}_{test}) \approx \sum f_\theta(\mathbf{X}, \mathbf{S}^{(i)}). \quad (21)$$

This theoretical property ensures that PathFinder can extrapolate to N -transmitter scenarios even when trained only on single-transmitter data, effectively addressing the distribution shift problem defined in Problem 2.

C. Gradient Smoothness of Momentum Prediction Loss

The proposed Momentum Prediction Loss (MPL) dynamically transitions between L_2 (MSE) and L_1 (MAE) loss based on an adaptive threshold δ . Let $r = \mathbf{Y} - \hat{\mathbf{Y}}$ be the residual. The gradient of MPL w.r.t prediction $\hat{\mathbf{Y}}$ is:

$$\frac{\partial \mathcal{L}}{\partial \hat{\mathbf{Y}}} = \begin{cases} -r, & |r| \leq \delta \\ -\delta \cdot \text{sign}(r), & |r| > \delta \end{cases} \quad (22)$$

Unlike standard Huber loss with a fixed δ , our momentum-updated δ_t adapts to the training dynamics. In the early stages, residuals $|r|$ are large. Since δ_t tracks the Mean Absolute Error (MAE), the gradient is clipped to δ_t , preventing exploding gradients commonly seen in MSE (where $\nabla \propto r$). As training converges and $|r| \rightarrow 0$, δ_t decreases, and the loss behaves like MSE, providing smooth gradients for fine-grained convergence. This adaptive mechanism ensures robust optimization across varying scales of path loss values.

VI. EXPERIMENT

A. Experimental Setup

To facilitate comparison with SOTA methods, we utilize the publicly available RadioMap3DSeer (RM3D) dataset [11]. RM3D accounts for varying building heights and transmitters deployed at different elevations, with these transmitters positioned at higher floors of the buildings. The dataset is generated through a combination of Intelligent Ray Tracing (IRT) and real-world maps, making it closely aligned with real-world applications [11]. After processing, the dataset comprises a total of 700 urban building maps, with each image representing an area of 256 m \times 256 m. All simulations are conducted at a minimum resolution of one meter, resulting in final images with dimensions of 256 \times 256 pixels. Additionally, each urban map considers 80 transmitter locations, culminating in a total of 56,000 simulations.

1) *Baseline*: AE [13], a convolutional autoencoder, predicts radio path loss. Its limited expressive capacity restricts its application to small datasets.

RadioUNet [9] was the first 2D radio path loss prediction algorithm. It models building and transmitter features separately, reducing UNet's training complexity. Easily adaptable to new 3D scenarios, it serves as an evaluation baseline.

PMNet [18], the current state of the art RPP algorithm, uses a pyramid structure for multi scale feature extraction and dilated convolutions to expand the model's receptive field.

Similarly, REM-Net [17] achieves precise RPP construction by expanding the receptive field and mitigating information loss. It employs multiple groups of dilated convolutions with varying kernel sizes to learn features at different scales.

2) *Evaluation Metric*: To evaluate the performance of different methods, we construct a total of six metrics. The first three metrics are global coverage metrics, namely MSE, RMSE, and NMSE. The latter three metrics focus on the receiver area and are referred to as MSE-R, RMSE-R, and NMSE-R. Due to space limitations, their calculation methods are provided in the appendix.

B. Comparison on DS-RPP

To compare model performance in DS-RPP scenarios, we partition the RadioMap3DSeer dataset into training, validation, and testing sets at a 5:1:1 ratio, based on sample order. This ensures distinct training and testing distributions.

Table I shows various models' performance on the testing set. Our model (PathFinder) outperforms others across both metrics, achieving SOTA results. It improves RMSE and RMSE-R metrics by 30.59% and 29.08% respectively, compared to REM-Net, significantly enhancing prediction performance in both global and local areas.

To intuitively analyze our model's superior performance, Fig. 3 displays prediction results for all baseline methods and our model across different samples. Each image row represents a sample. The first column shows building and transmitter locations (red dots), the second illustrates ideal path loss prediction, and subsequent columns present predictions from different models, annotated with their respective MSE scores below. For clarity, we highlight important image areas with red boxes. Unedited original images are in the appendix.

The AE model's limited receptive field leads to weak predictive capability for distant regions, as seen in Inputs 1 and 2. It also primarily focuses on areas near the transmitter (Input 5), making it the poorest performer among all models.

RadioUNet and PMNet show similar performance with minimal MSE differences. Both struggle with path loss predictions along building edges (Inputs 3, 4, and 5), where predictions around contours appear vague, lacking clear boundaries. PMNet's more complex architecture makes it more prone to overfitting, leading to blurrier predictions in distribution shift scenarios than RadioUNet. Thus, despite PMNet's lower MSE loss, its distribution shift handling ability is comparable to RadioUNet's.

REM-Net is the best-performing baseline, successfully establishing basic path loss boundaries in all samples. However,

its boundary delineation lacks the precision of our proposed model. For instance, in Inputs 1 and 5, path loss regions farther from the transmitter show suboptimal clarity, while our model exhibits more distinct boundaries. This improvement stems from the attention mechanism's ability to learn global features, allowing the model to focus on features from distant locations. Additionally, in Input 2, REM-Net's path loss estimation on the building side away from the transmitter is insufficiently accurate. In complex building distribution areas, our model surpasses REM-Net, as seen in the red boxes of Inputs 3 and 4, where multiple buildings are present and our model's path loss boundaries are clearer.

To numerically substantiate this observation, we plotted the cumulative distribution of predicted path loss probabilities for all models across these samples, as shown in Fig. 4. The AE model shows significant discrepancies between predictions and actual ground truth across different path loss intervals, achieving performance close to true labels only with simpler building distributions (e.g., sample 5).

Moreover, RadioUNet, PMNet, and REM-Net struggle with accurate predictions in the 0 to 0.25 path loss range. This range precisely corresponds to high frequency image information. Thus, despite numerically close MSE losses, perceptual differences are substantial. In contrast, PathFinder consistently performs closer to the true path loss in high frequency regions across most samples, leading to a marked improvement in perceptual accuracy.

TABLE I: Comparison of different models' performance DS-RPP. **Bold** indicates the best model, while underline indicates the second-best model.

Model	MSE	RMSE	NMSE	MSE-R	RMSE-R	NMSE-R
AE	0.00478	0.069131	0.043575	0.005159	0.071818	0.038498
RadioUNet	0.003252	0.057026	0.029639	0.003313	0.057552	0.024713
PMNet	0.002399	0.048977	0.021872	0.002504	0.050035	0.018685
REM-Net	0.002272	0.047644	0.020729	0.002305	0.047994	0.017217
PathFinder	0.001096	<u>0.033069</u>	<u>0.010004</u>	0.001161	<u>0.03404</u>	0.008673

C. Coverage Analysis

In practical scenarios, models often only need to accurately predict critical areas. Regions with low signal strength can be considered noise [9]. Inspired by previous work [9], we analyze model performance differences by visualizing a subset of samples. We consider the most important 40%, 30%, 20%, and 5% of path loss, respectively.

Table II presents all models' performance regarding critical path loss area coverage. The final column shows our model's relative improvement over the second best model. As the importance factor increases (from 40% to 5%), PathFinder's advantages become more pronounced. For the 40% most important coverage area, performance improves by 34.46% over REM-Net. For only the 5% most important coverage area, PathFinder outperforms REM-Net by 52.38%. This demonstrates our model significantly enhances path loss prediction accuracy across different importance ratios.

Practically, predictions typically focus on the 20% most important areas. Therefore, we visualize and analyze this scenario, as shown in Fig. 5. Visualizations for other importance levels appear in the appendix.

Inputs 1, 2, and 4 show that only PathFinder predicts clear boundaries in areas farther from the transmitter. Other models, like AE and RadioUNet, exhibit substantial boundary prediction deficiencies. In complex building distribution areas (Input 3), only REM-Net and PathFinder accurately predict path loss. Other models fail to estimate path loss in these complex regions. For Input 5, models struggle with path loss predictions on the building side away from the transmitter. This is due to complex physical principles of signal propagation. REM-Net performs best among baselines, but its high frequency component predictions still fall short of PathFinder. PathFinder shows a 51.87% improvement, resulting in predictions perceptually closer to ground truth.

TABLE II: RMSE comparison of different models when addressing coverage areas of varying importance.

Coverage/Model	AE	RadioUNet	PMNet	REM-Net	Ours	Improvement
40	0.1249	0.0849	0.0756	0.0582	0.0382	34.46%
30	0.1107	0.0717	0.0639	<u>0.0477</u>	0.0292	38.77%
20	0.0721	0.0545	0.0488	<u>0.0350</u>	0.0197	43.72%
10	0.0299	0.0306	0.0280	<u>0.0188</u>	0.0098	48.09%
5	0.0142	0.0158	0.0150	<u>0.0096</u>	0.0046	52.38%

D. Comparison on S2MT-RPP

To analyze model performance with multiple transmitters, we first established a DS-RPP task with two transmitters by fixing the parameter $\beta = 0.5$ in Eq. (16) and omitting image enhancement. To further assess performance with varying transmitter counts, we modified Eq. (16) to average the effects of any number of S_i and Y_i for S2MT-RPP. We evaluated models with 2 to 5 transmitters, presenting RMSE results in Table III and visualizing cases with 2 and 4 transmitters in Figs. 6 and 7, respectively.

Table III shows that while baseline models like AE and RadioUNet experience increased loss and performance decline as transmitter count rises, more advanced models like PMNet and REM-Net maintain relatively consistent performance. Our model, however, demonstrates remarkable consistency across all transmitter counts, achieving a 59.35% improvement over REM-Net even with five transmitters. This highlights the effectiveness of the proposed TOM strategy in enhancing our model's performance in distribution shift scenarios and its robust zero-shot capabilities.

Fig. 6 (2 transmitters) illustrates that when transmitters are close and unobstructed (Sample 1), most models (except AE) perform similarly. However, with complex building distributions, distant transmitters, or obstructions (Sample 2), RadioUNet and PMNet fail to accurately predict path loss in densely built areas and often only predict the effect of a single transmitter (Sample 3). REM-Net faces similar challenges, struggling with path loss predictions near transmitters in complex regions.

When the number of transmitters increases to four (Fig. 7), the generalization capabilities of all baseline models, particularly AE and RadioUNet, largely fail. PMNet and REM-Net perform relatively better but still struggle to predict clear path loss boundaries even in straightforward building scenarios. In

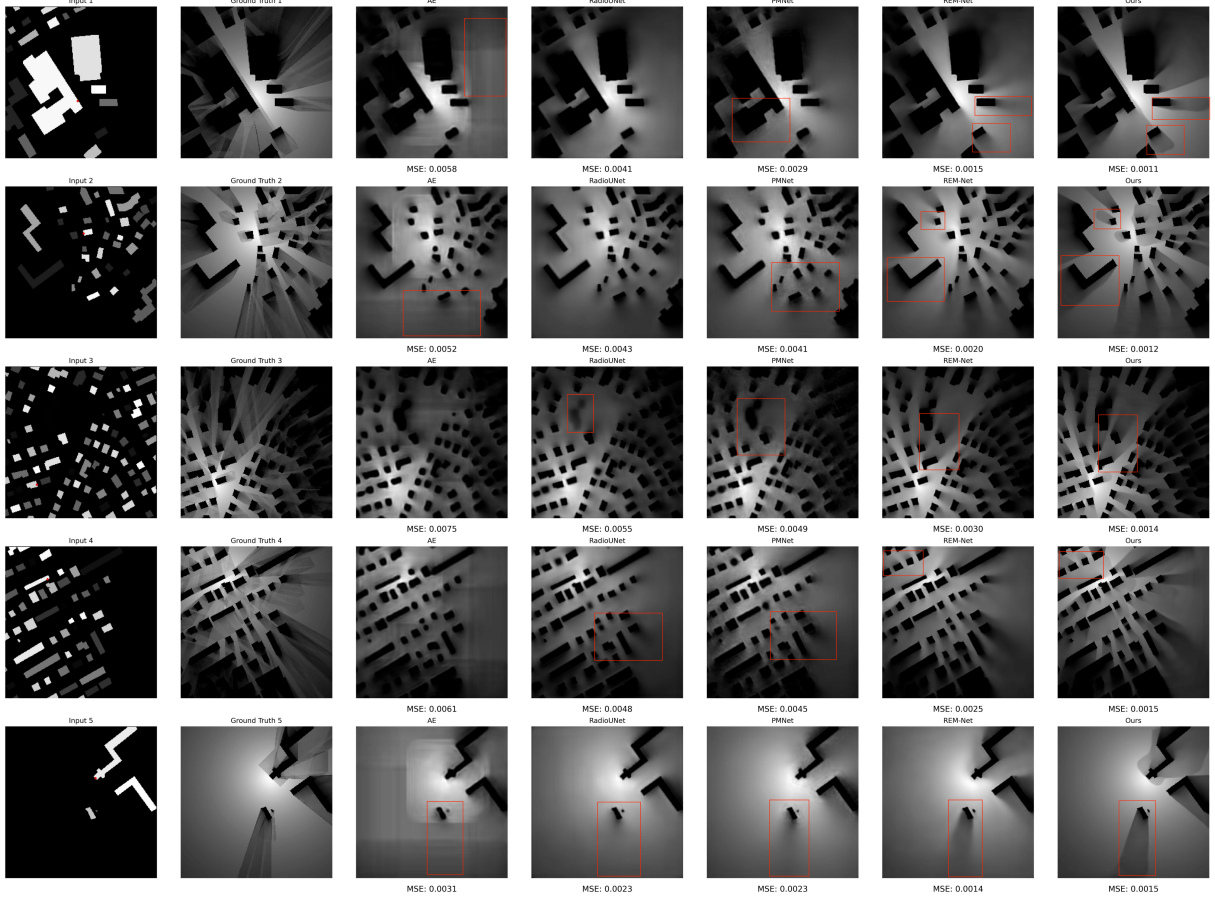


Fig. 3: Visualization examples of different models in the DS-RPP task.

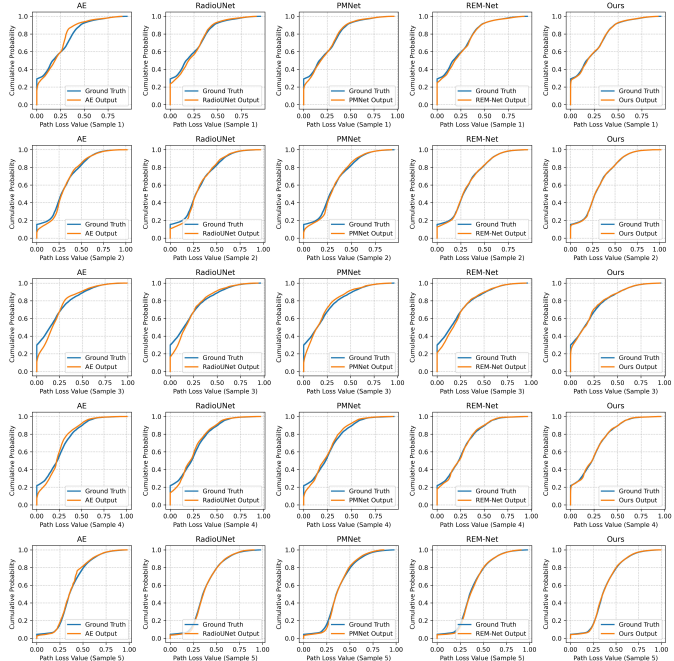


Fig. 4: Cumulative distribution plots of predicted probabilities for different models.

contrast, PathFinder maintains a certain clarity in path loss boundaries across various situations, achieving a very low MSE of 0.0006 in simpler building distributions (Sample 1), indicating close alignment with true targets.

In summary, while current SOTA models show some ability to handle distribution shifts and exhibit zero-shot performance in multi-transmitter scenarios, their generalization in complex building distributions or with multiple transmitters is significantly inferior to that of PathFinder.

TABLE III: Comparison of different models' performance under distribution shifts caused by varying numbers of transmitters.

Tx-Num/Model	AE	RadioUNet	PMNet	REM-Net	Ours	Improvement
2	0.091157	0.097661	0.090341	0.090515	0.03075	65.97%
3	0.114313	0.158482	0.092957	0.083091	0.02873	65.43%
4	0.128223	0.176148	0.088597	0.075713	0.02837	62.53%
5	0.134286	0.179481	0.082717	0.070813	0.02879	59.35%

E. Convergence Analysis of Different Models

To further investigate the reasons behind the differences in distribution shift handling capabilities across various models and to demonstrate that the proposed MPL optimization effectively aids model convergence, we analyze the convergence processes of different models. Fig. 8 illustrates the changes in loss for all models during training and validation. "Ours

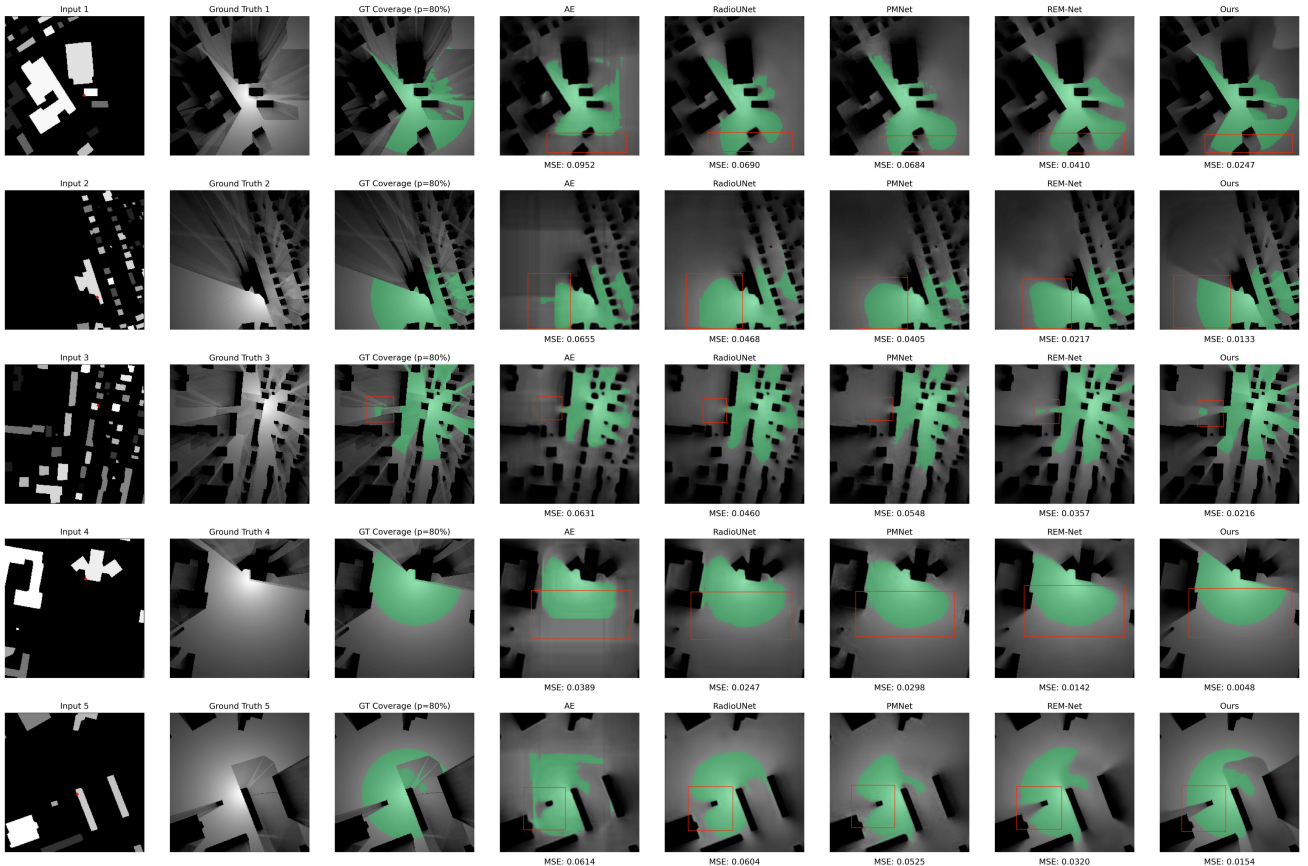


Fig. 5: Visualization cases of different models when dealing with the most important 20% of the coverage area.

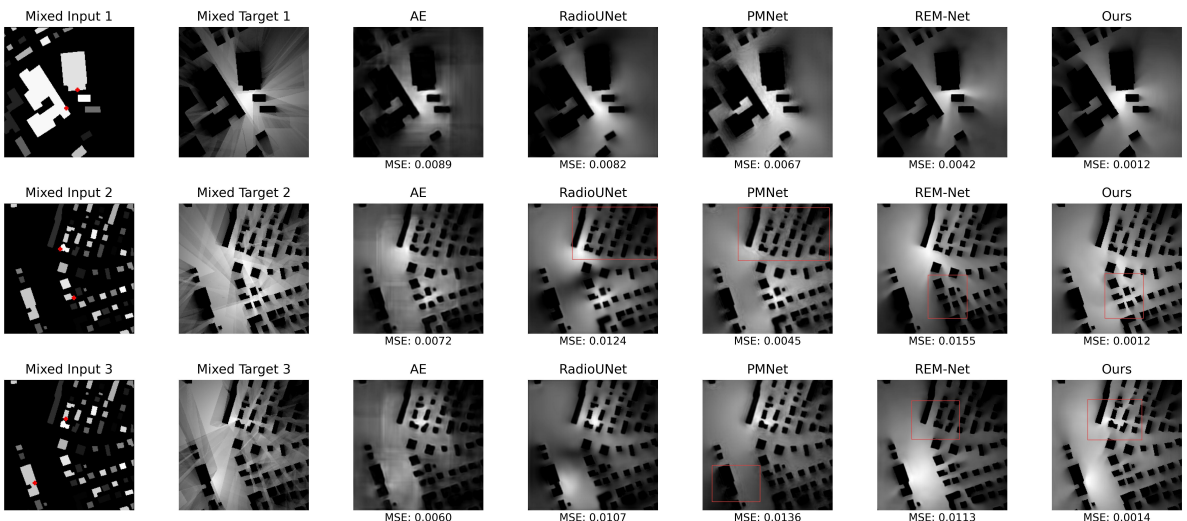


Fig. 6: Visualization of performance of different models when the number of transmitters is 2.

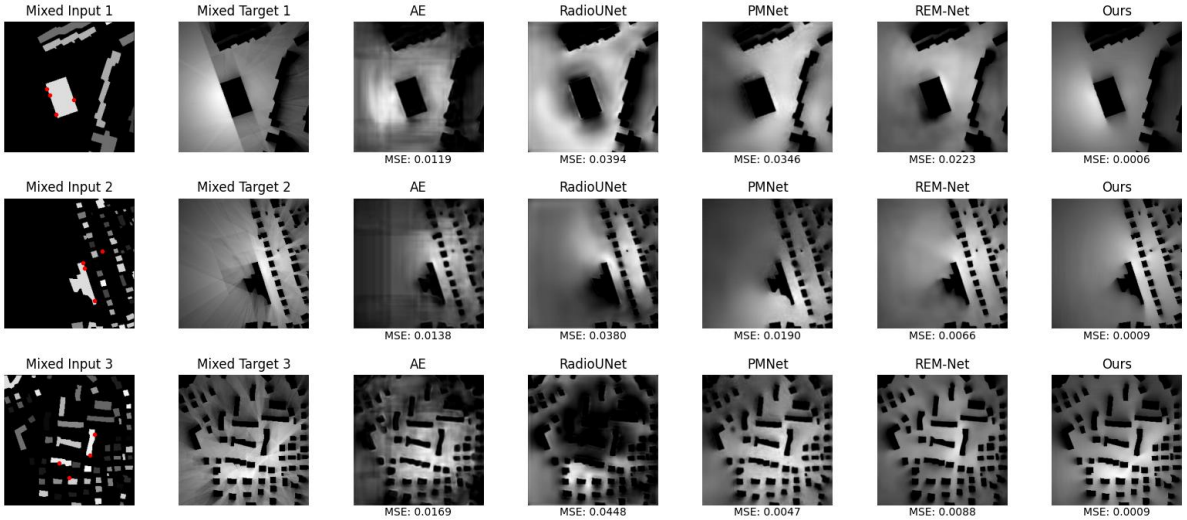


Fig. 7: Visualization of performance of different models when the number of transmitters is 4.

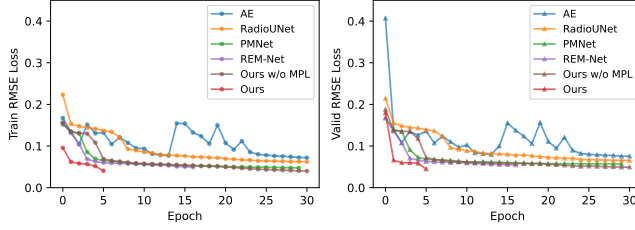


Fig. 8: Variation of RMSE loss during the training and validation phases across different models.

“w/o MPL” represents our model without MPL optimization, wherein MSE is used as a substitute loss for model optimization. In implementation, we set a maximum of 30 training epochs and employed an early stopping strategy, saving the best model when the validation loss no longer decreases. In our experiments, our model, along with PMNet and REM-Net, triggered this strategy.

From Fig. 8, it is evident that the AE model exhibits considerable fluctuations in loss during training, while the other models show minimal fluctuations. Additionally, REM-Net converges the fastest among all models, with a noticeable slowdown in loss reduction approximately after 3 epochs. Before utilizing MPL, the convergence speed of “Ours w/o MPL” is comparable to that of PMNet, with a similar slowdown in loss reduction after 5 epochs. After the implementation of MPL, our model demonstrates the fastest convergence rate among all models, achieving the lowest validation loss and quickly triggering the early stopping mechanism. This validates the effectiveness of MPL in significantly enhancing model convergence speed and enabling the model to reach lower loss values.

VII. CONCLUSION

This paper addresses 5G path loss estimation, extending to out of distribution prediction with multiple transmitters.

Addressing prior research gaps, including insufficient environmental modeling, a single transmitter focus, and neglected out of distribution path loss prediction, we introduce PathFinder. This model decouples building and transmitter features for active environmental modeling. It employs mask guided low rank attention to learn global environmental features, independently focusing on the decoupled features. Furthermore, we establish a novel S2MT-RPP task with the proposed Transmitter Oriented Mixup method. We empirically analyze various models’ performance on this task and the reasons for suboptimal results. Experiments show that PathFinder achieves state of the art performance across multiple distribution shift scenarios, showcasing robust generalization and zero shot capabilities. Future work aims to explore more real world tasks with the proposed model, treating it as a foundational model to address practical challenges.

ACKNOWLEDGMENTS

This work was supported in part by National Natural Science Foundation of China No. 92467109, U21A20478, National Key R&D Program of China 2023YFA1011601, and the Major Key Project of PCL, China under Grant PCL2025A11 and PCL2025A13.

REFERENCES

- [1] D. Zhang, Y. Lu, Y. Li, W. Ding, B. Zhang, and J. Xiao, “Frequency learning attention networks based on deep learning for automatic modulation classification in wireless communication,” *Pattern Recognition*, vol. 137, p. 109345, 2023.
- [2] C.-H. Ko and S.-H. Wu, “A framework for proactive indoor positioning in densely deployed wifi networks,” *IEEE Transactions on Mobile Computing*, vol. 21, no. 1, pp. 1–15, 2022.
- [3] S. Sorour, Y. Lostanlen, S. Valaee, and K. Majeed, “Joint indoor localization and radio map construction

with limited deployment load,” *IEEE Transactions on Mobile Computing*, vol. 14, no. 5, pp. 1031–1043, 2015.

[4] K. Majeed, S. Sorour, T. Y. Al-Naffouri, and S. Valaee, “Indoor localization and radio map estimation using unsupervised manifold alignment with geometry perturbation,” *IEEE Transactions on Mobile Computing*, vol. 15, no. 11, pp. 2794–2808, 2016.

[5] T. T. Oladimeji, P. Kumar, and N. O. Oyie, “Propagation path loss prediction modelling in enclosed environments for 5g networks: A review,” *Heliyon*, vol. 8, no. 11, 2022.

[6] J. Isabona, A. L. Imoize, S. Ojo, O. Karunwi, Y. Kim, C.-C. Lee, and C.-T. Li, “Development of a multilayer perceptron neural network for optimal predictive modeling in urban microcellular radio environments,” *Applied Sciences*, vol. 12, no. 11, p. 5713, 2022.

[7] H. Zhang, Y. Han, L. Meng, G. Gui, W. Xiang, and Y. Lin, “Mffgcn: Multimodal feature fusion graph convolution network for radio map estimation with uneven spatial sampling,” *IEEE Transactions on Mobile Computing*, vol. 24, no. 12, pp. 13 366–13 382, 2025.

[8] S. Shao, L. Cheng, K. Chen, Q. Liu, S. Zhang, H. Zhang, and L. Song, “Collaboradio: A hybrid device-edge-cloud collaboration paradigm for fine-grained radio map construction,” *IEEE Transactions on Mobile Computing*, vol. 25, no. 1, pp. 599–613, 2026.

[9] R. Levie, C. Yapar, G. Kutyniok, and G. Caire, “RadioUNet: Fast Radio Map Estimation With Convolutional Neural Networks,” *IEEE Transactions on Wireless Communications*, vol. 20, no. 6, pp. 4001–4015, Jun. 2021.

[10] X. Wang, K. Tao, N. Cheng, Z. Yin, Z. Li, Y. Zhang, and X. Shen, “RadioDiff: An Effective Generative Diffusion Model for Sampling-Free Dynamic Radio Map Construction,” *IEEE Transactions on Cognitive Communications and Networking*, pp. 1–1, 2024.

[11] C. Yapar, F. Jaensch, R. Levie, G. Kutyniok, and G. Caire, “Overview of the first pathloss radio map prediction challenge,” *IEEE Open Journal of Signal Processing*, vol. 5, pp. 948–963, 2024.

[12] N. Moraitis, L. Tsipi, D. Vouyioukas, A. Gkioni, and S. Louvros, “Performance evaluation of machine learning methods for path loss prediction in rural environment at 3.7 ghz,” *Wireless networks*, vol. 27, no. 6, pp. 4169–4188, 2021.

[13] Y. Teganya and D. Romero, “Deep completion autoencoders for radio map estimation,” *IEEE Transactions on Wireless Communications*, vol. 21, no. 3, pp. 1710–1724, 2022.

[14] A. Chaves-Villota and C. A. Viteri-Mera, “DeepREM: Deep-Learning-Based Radio Environment Map Estimation From Sparse Measurements,” *IEEE Access*, vol. 11, pp. 48 697–48 714, 2023.

[15] K. Qiu, S. Bakirtzis, H. Song, J. Zhang, and I. Wassell, “Pseudo ray-tracing: Deep leaning assisted outdoor mm-wave path loss prediction,” *IEEE Wireless Communications Letters*, vol. 11, no. 8, pp. 1699–1702, 2022.

[16] S. P. Sotiroudis, P. Sarigiannidis, S. K. Goudos, and K. Siakavara, “Fusing diverse input modalities for path loss prediction: A deep learning approach,” *Ieee Access*, vol. 9, pp. 30 441–30 451, 2021.

[17] Q. Chen, M. Huang, and J. Yang, “Rem-net+: 3d radio environment map construction guided by radio propagation model,” *Authorea Preprints*, 2024.

[18] J.-H. Lee, J. Lee, S.-H. Lee, and A. F. Molisch, “PM-Net: Large-Scale Channel Prediction System for ICASSP 2023 First Pathloss Radio Map Prediction Challenge,” in *ICASSP 2023 - 2023 IEEE International Conference on Acoustics, Speech and Signal Processing (ICASSP)*, Jun. 2023, pp. 1–2, iSSN: 2379-190X.

[19] O. Ronneberger, P. Fischer, and T. Brox, “U-net: Convolutional networks for biomedical image segmentation,” in *Medical image computing and computer-assisted intervention–MICCAI 2015: 18th international conference, Munich, Germany, October 5-9, 2015, proceedings, part III 18*. Springer, 2015, pp. 234–241.

[20] A. Doshi, J. Namgoong, and T. Yoo, “Radio DIP - Completing Radio Maps using Deep Image Prior,” in *GLOBECOM 2023 - 2023 IEEE Global Communications Conference*. Kuala Lumpur, Malaysia: IEEE, Dec. 2023, pp. 1543–1548.

[21] Z. Yu, Z. Zhong, K. Yang, W. Cao, and C. P. Chen, “Broad learning autoencoder with graph structure for data clustering,” *IEEE Trans. Knowl. Data Eng.*, 2023.

[22] X. Xi, Y. Huang, Z. Zhong, and R. Luo, “Umb: Understanding model behavior for open-world object detection,” *Advances in Neural Information Processing Systems*, vol. 37, pp. 74 233–74 261, 2024.

[23] Z. Zhong, K. Yang, Z. Yu, Y. Shi, and C. L. Philip Chen, “Towards efficient anomaly detection using memory broad learning system,” in *2023 9th International Conference on Control Science and Systems Engineering (ICCSSE)*, 2023, pp. 252–257.

[24] C. Yapar, R. Levie, G. Kutyniok, and G. Caire, “Real-time outdoor localization using radio maps: A deep learning approach,” *IEEE Transactions on Wireless Communications*, vol. 22, no. 12, pp. 9703–9717, 2023.

[25] F. Mitchell, A. Bhaskara, J. Wang, and N. Patwari, “Less is more: Improved path loss prediction using simple interpolation models,” in *2024 IEEE International Symposium on Dynamic Spectrum Access Networks (DySPAN)*, 2024, pp. 139–144.

[26] J. L. Ba, J. R. Kiros, and G. E. Hinton, “Layer normalization,” *arXiv preprint arXiv:1607.06450*, 2016.

[27] J. Xu, X. Sun, Z. Zhang, G. Zhao, and J. Lin, “Understanding and improving layer normalization,” *Advances in neural information processing systems*, vol. 32, 2019.

[28] A. Vaswani, N. Shazeer, N. Parmar, J. Uszkoreit, L. Jones, A. N. Gomez, L. u. Kaiser, and I. Polosukhin, “Attention is all you need,” in *Advances in Neural Information Processing Systems*, I. Guyon, U. V. Luxburg, S. Bengio, H. Wallach, R. Fergus, S. Vishwanathan, and R. Garnett, Eds., vol. 30. Curran Associates, Inc., 2017.

[29] R. Fan, T. He, and M. Dong, “Multi-faceted data augmentation for aspect-based sentiment analysis via large language models,” *Knowledge-Based Systems*, vol. 331, p. 114827, 2026.

[30] P. Zhao, J. Shi, P. Ye, H. Liu, and X. Ji, “Robust label

propagation based on prior-guided cross domain data augmentation for few-shot unsupervised domain adaptation,” *Knowledge-Based Systems*, vol. 329, p. 114432, 2025.

[31] H. Zhang, H. Hu, B. Cao, and X. Zhang, “Auto-stylemixer: A universal adaptive n-to-one framework for cross-domain data augmentation,” *Knowledge-Based Systems*, vol. 323, p. 113616, 2025.

[32] S.-A. Rebuffi, S. Gowal, D. A. Calian, F. Stimberg, O. Wiles, and T. A. Mann, “Data augmentation can improve robustness,” *Advances in neural information processing systems*, vol. 34, pp. 29 935–29 948, 2021.

[33] I. F. Akyildiz, Z. Sun, and M. C. Vuran, “Signal propagation techniques for wireless underground communication networks,” *Physical Communication*, vol. 2, no. 3, pp. 167–183, 2009.

[34] C. Hens, U. Harush, S. Haber, R. Cohen, and B. Barzel, “Spatiotemporal signal propagation in complex networks,” *Nature Physics*, vol. 15, no. 4, pp. 403–412, 2019.

[35] P. Li, Z. Zhong, T. Zhang, Z. Yu, C. Chen, and K. Yang, “A new perspective on time series anomaly detection: Faster patch-based broad learning system,” *arXiv preprint arXiv:2412.05498*, 2024.

[36] Z. Zhong, Z. Yu, Z. Fan, C. L. Philip Chen, and K. Yang, “Adaptive memory broad learning system for unsupervised time series anomaly detection,” *IEEE Transactions on Neural Networks and Learning Systems*, vol. 36, no. 5, pp. 8331–8345, 2025.

[37] Z. Zhong, Z. Yu, X. Xi, Y. Xu, W. Cao, Y. Yang, K. Yang, and J. You, “Simad: A simple dissimilarity-based approach for time-series anomaly detection,” *IEEE Transactions on Neural Networks and Learning Systems*, vol. 36, no. 11, pp. 19 669–19 680, 2025.

[38] Z. Zhong, Z. Yu, J. Chen, and K. Yang, “Insightful simplicity: Dissimilarity in time series anomaly detection,” in *Proceedings of the ACM Turing Award Celebration Conference - China 2024*, ser. ACM-TURC ’24. New York, NY, USA: Association for Computing Machinery, 2024, p. 242–243.

A. EXPERIMENT

A. Evaluation Metric

To evaluate the performance of different methods, we construct a total of six core metrics. The first three metrics are global coverage metrics, namely MSE, RMSE, and NMSE. The latter three metrics focus on the receiver area and are referred to as MSE-R, RMSE-R, and NMSE-R.

Global Coverage Metrics 1. Mean Squared Error (MSE) serves as a fundamental accuracy metric, directly reflecting the model's prediction error across the entire area. The calculation formula is given by:

$$\text{MSE} = \frac{1}{HW} \sum_{i=1}^{HW} (\mathbf{Y}_i - \hat{\mathbf{Y}}_i)^2, \quad (23)$$

where \mathbf{Y}_i and $\hat{\mathbf{Y}}_i$ represent the true value and predicted value of the i -th pixel, respectively, and HW is the total number of pixels in the entire area. This metric amplifies the influence of outliers by taking the arithmetic mean of the squared errors, measuring the overall fitting error of the model across the entire study area.

2. Root Mean Squared Error (RMSE) normalizes the dimensions based on MSE, expressed as:

$$\text{RMSE} = \sqrt{\frac{1}{HW} \sum_{i=1}^{HW} (\mathbf{Y}_i - \hat{\mathbf{Y}}_i)^2}, \quad (24)$$

This metric shares the same dimension as the true values, providing an intuitive reflection of the average deviation between the predicted and true values, making it more interpretable than MSE.

3. Normalized Mean Squared Error (NMSE) eliminates the dimensional influence through relative error representation, defined as:

$$\text{NMSE} = \frac{\sum_{i=1}^{HW} (\mathbf{Y}_i - \hat{\mathbf{Y}}_i)^2}{\sum_{i=1}^{HW} \mathbf{Y}_i^2}. \quad (25)$$

This metric transforms absolute errors into relative errors, making it more suitable for assessing scenarios with significant differences in path loss.

Receiver Area-based Metrics: The last three metrics focus on the receiver area $\mathcal{M}' \in \{0, 1\}^{HW \times 1}$ (where $\mathcal{M}'_i = 1$ indicates the i -th pixel belongs to the receiver area), enabling targeted evaluation of the specified region through a mask matrix. The specific forms correspond to the basic metrics but introduce area weights.

1. Mean Squared Error for Receiver (MSE-R):

$$\text{MSE-R} = \frac{1}{|\mathcal{M}'|} \sum_{i=1}^{HW} \mathcal{M}'_i \cdot (\mathbf{Y}_i - \hat{\mathbf{Y}}_i)^2, \quad (26)$$

where $|\mathcal{M}'|$ denotes the total number of valid pixels in the receiver area (i.e., the number of pixels where $\mathcal{M}'_i = 1$). This metric focuses on fitting errors in the receiver area through masked weighted averages, amplifying the influence of outliers in the target region.

2. Root Mean Squared Error for Receiver (RMSE-R):

$$\text{RMSE-R} = \sqrt{\frac{1}{|\mathcal{M}'|} \sum_{i=1}^{HW} \mathcal{M}'_i \cdot (\mathbf{Y}_i - \hat{\mathbf{Y}}_i)^2} = \sqrt{\text{MSE-R}}. \quad (27)$$

This metric normalizes dimensions based on MSE-R, aligning with the dimensions of the true values to intuitively reflect the average deviation between the predicted values and true values in the receiver area.

3. Normalized Mean Squared Error for Receiver (NMSE-R):

$$\text{NMSE-R} = \frac{\sum_{i=1}^{HW} \mathcal{M}'_i \cdot (\mathbf{Y}_i - \hat{\mathbf{Y}}_i)^2}{\sum_{i=1}^{HW} \mathcal{M}'_i \cdot \mathbf{Y}_i^2}. \quad (28)$$

This metric calculates relative errors in the receiver area, eliminating dimensional influences and normalizing regional differences, making it suitable for comparing model performance across different receiver scenarios.

In summary, the first category of global coverage metrics not only requires the model to focus on RPP estimation but also evaluates the model's overall fitting capability. In contrast, the second category of receiver area extended metrics solely considers the model's RPP ability, making it more task-specific.

B. Comparison on DS-RPP

Fig. A9 displays the prediction results of all baseline methods alongside our model across different samples.

C. Coverage Analysis

Figs. A10, A11, A12, A13 and A14 visualize the results of different models when the importance of the coverage area is 40%, 30%, 20%, 10% and 5%, respectively.

TABLE A4: Comparison of different models' performance under distribution shifts caused by varying numbers of transmitters.

Tx-num/Model	Metric	AE	RadioUNet	PMNet	REM-Net	Ours	Improvement
2	MSE	0.008311	0.009541	0.008171	0.008204	0.00095	88.43%
	RMSE	0.091157	0.097661	0.090341	0.090515	0.03075	65.97%
	NMSE	0.133632	0.15345	0.131345	0.131917	0.0152	88.43%
3	MSE	0.01307	0.025124	0.008654	0.006909	0.000825	88.05%
	RMSE	0.114313	0.158482	0.092957	0.083091	0.028727	65.43%
	NMSE	0.220913	0.424658	0.146268	0.116794	0.013955	88.05%
4	MSE	0.016445	0.031034	0.00786	0.005737	0.000805	85.97%
	RMSE	0.128223	0.176148	0.088597	0.075713	0.028369	62.53%
	NMSE	0.28556	0.538926	0.136471	0.099624	0.013983	85.96%
5	MSE	0.018037	0.032217	0.00685	0.005018	0.00083	83.48%
	RMSE	0.134286	0.179481	0.082717	0.070813	0.02879	59.35%
	NMSE	0.318152	0.568353	0.120816	0.088533	0.01463	83.48%

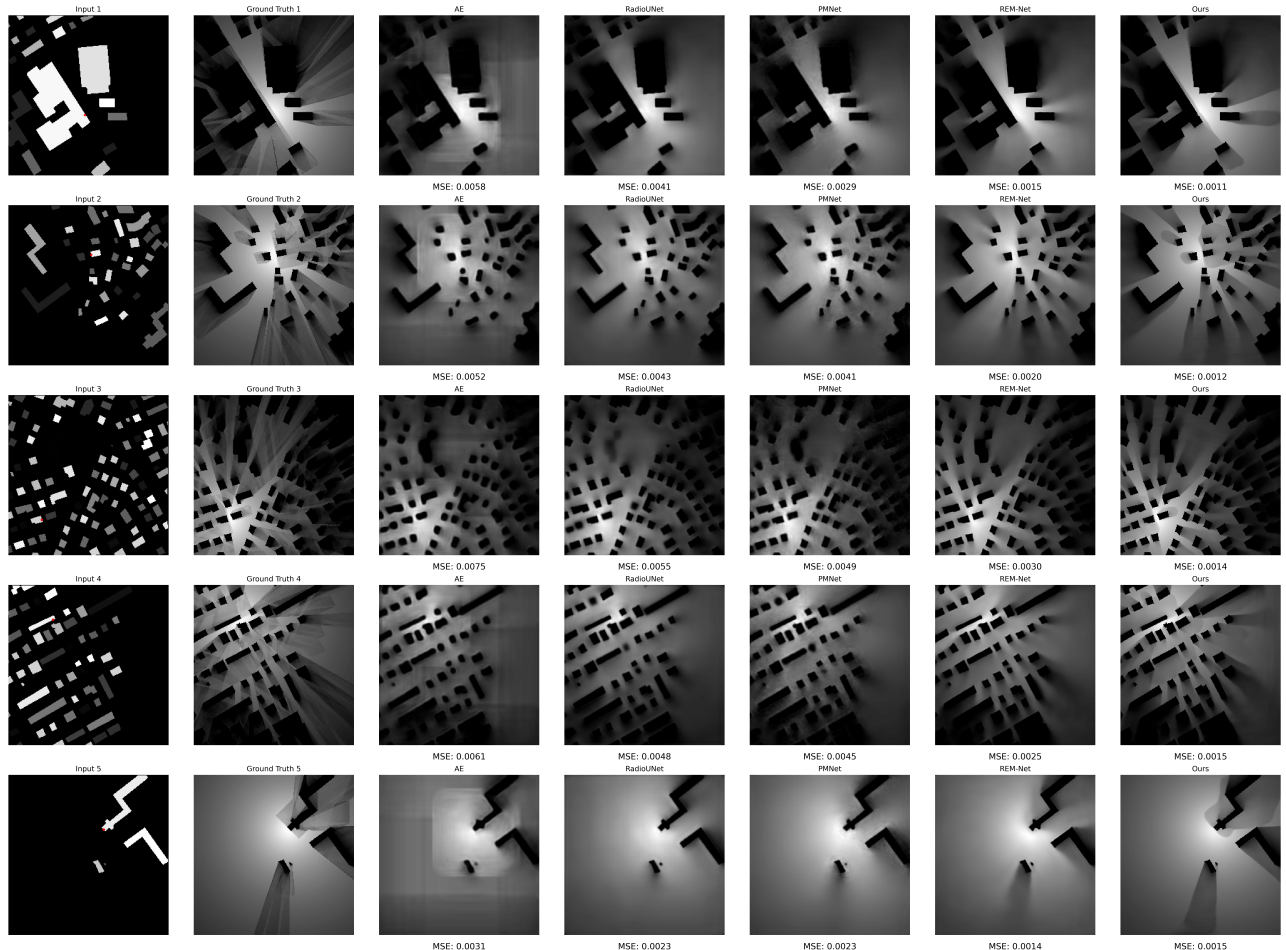


Fig. A9: Visualization examples of different models in the DS-RPP task.

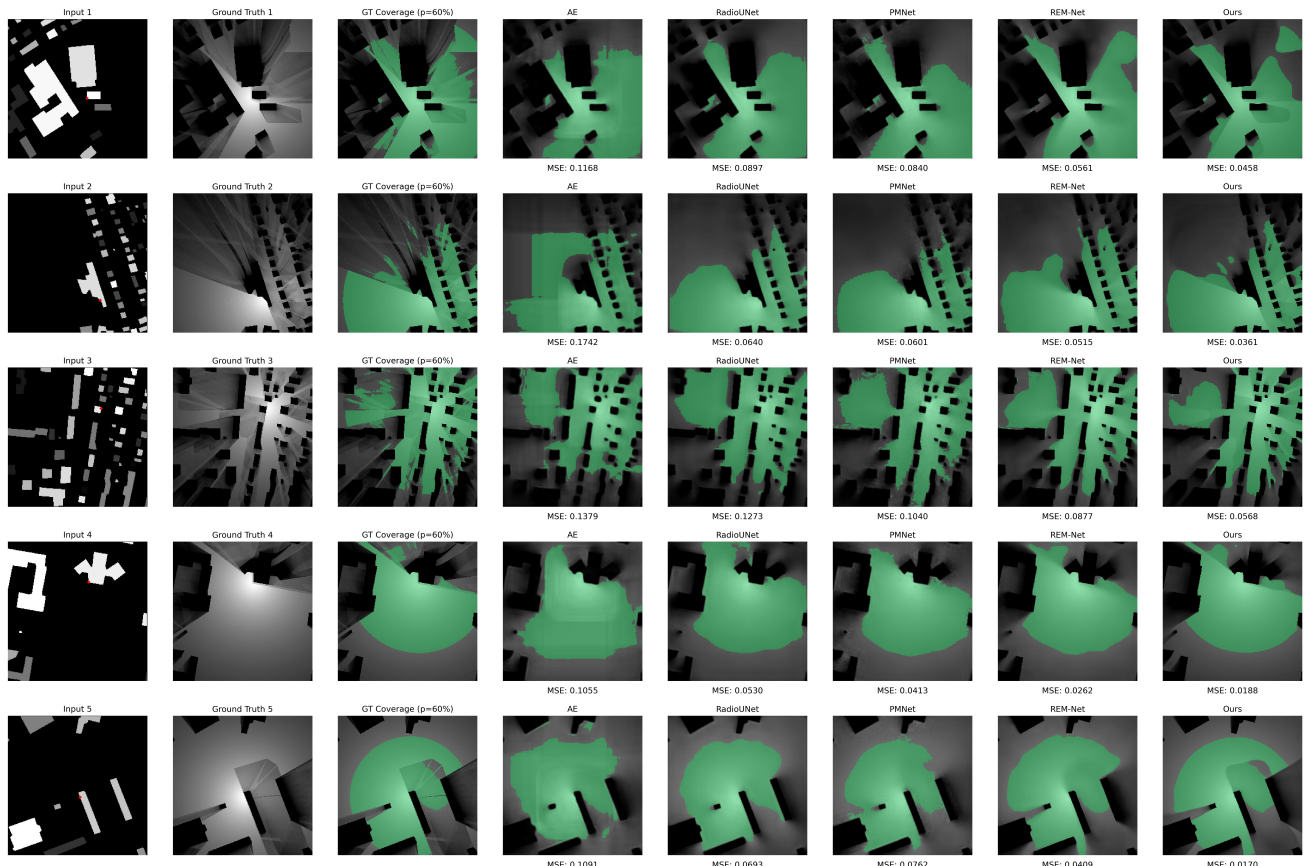


Fig. A10: Visualization cases of different models when dealing with the most important 40% of the coverage area.

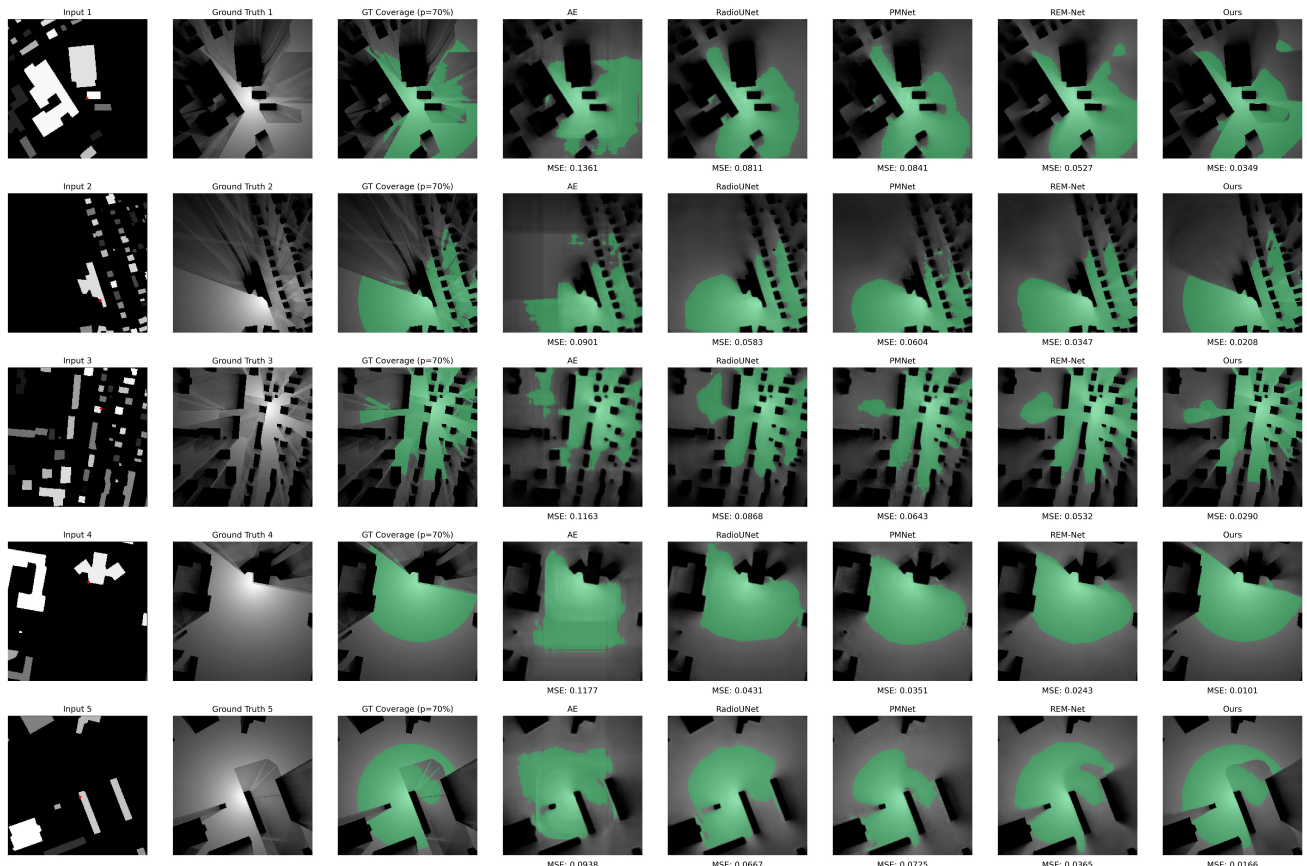


Fig. A11: Visualization cases of different models when dealing with the most important 30% of the coverage area.

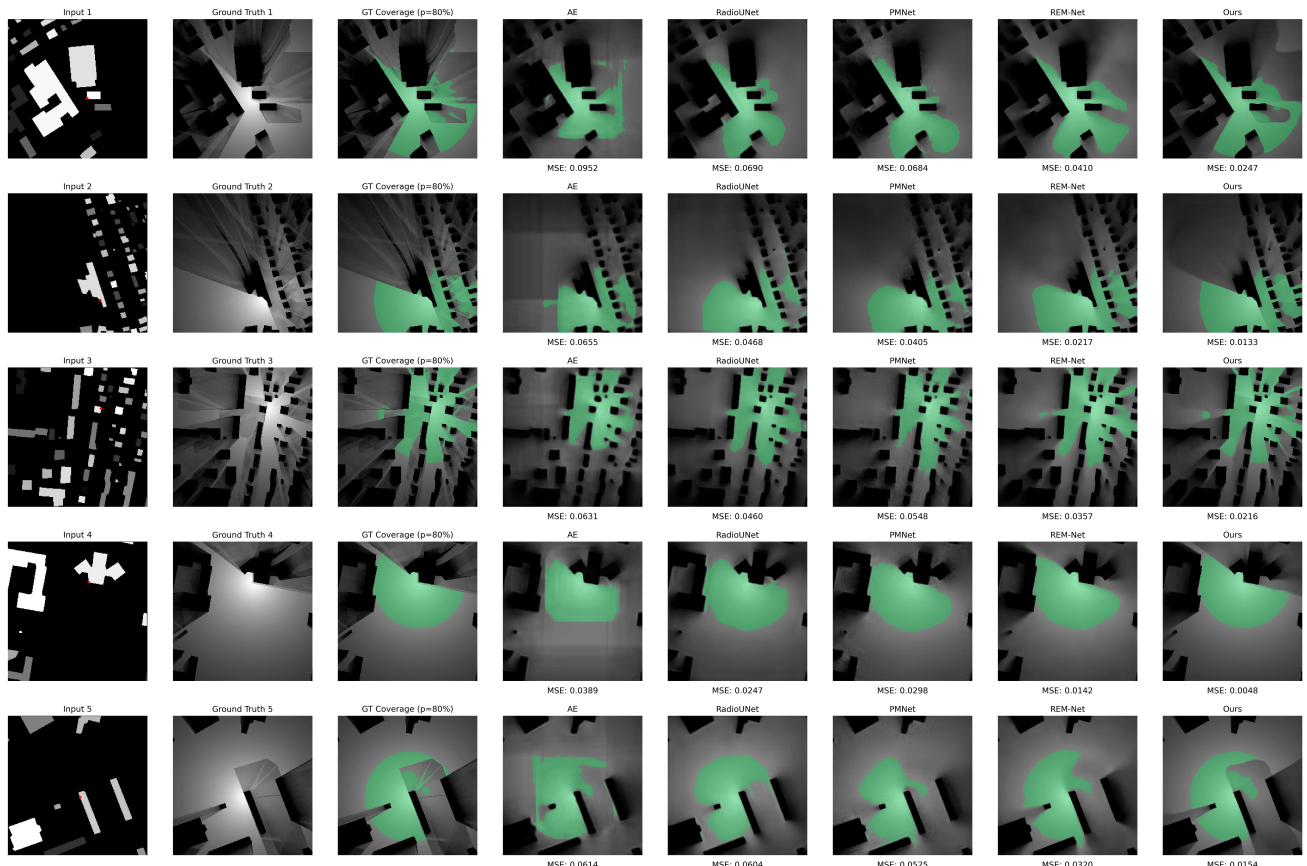


Fig. A12: Visualization cases of different models when dealing with the most important 20% of the coverage area.

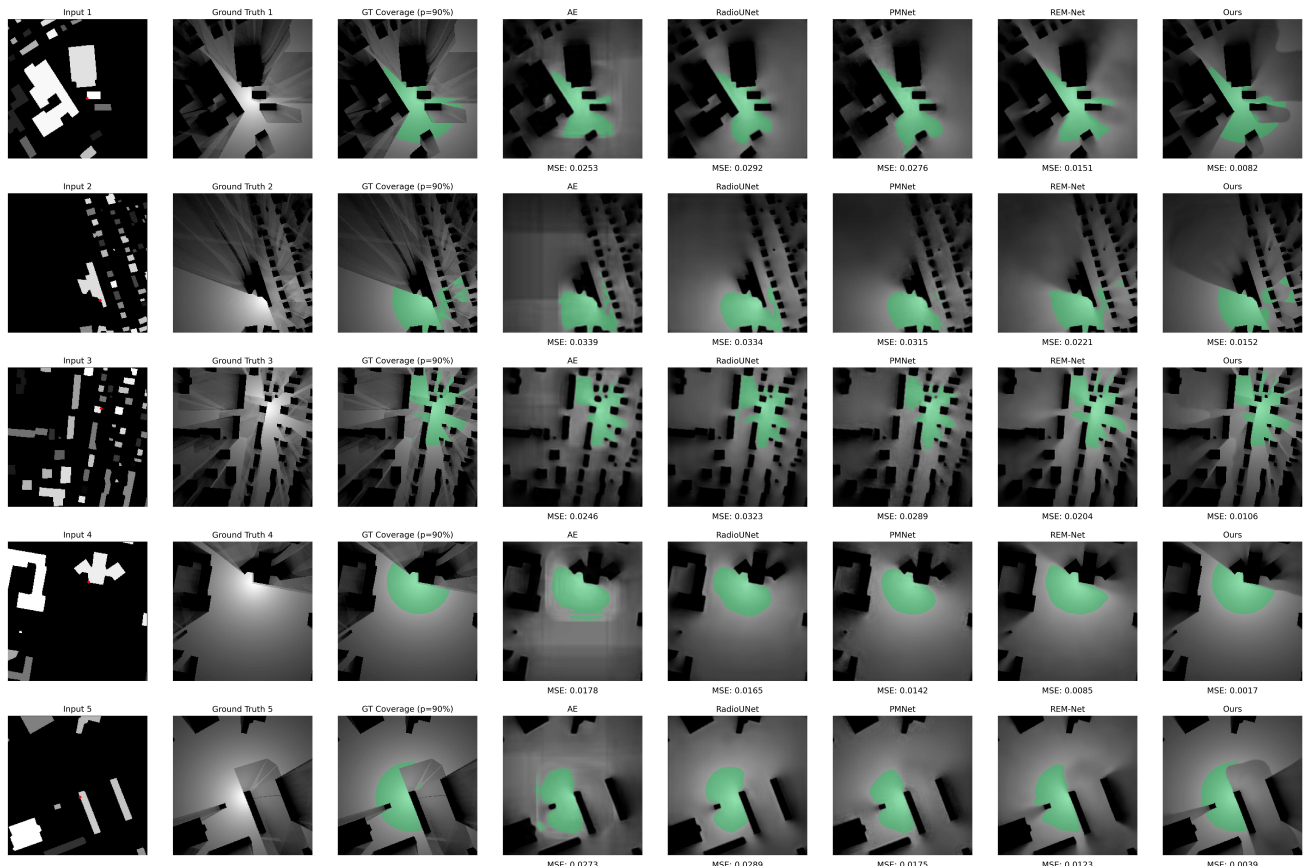


Fig. A13: Visualization cases of different models when dealing with the most important 10% of the coverage area.

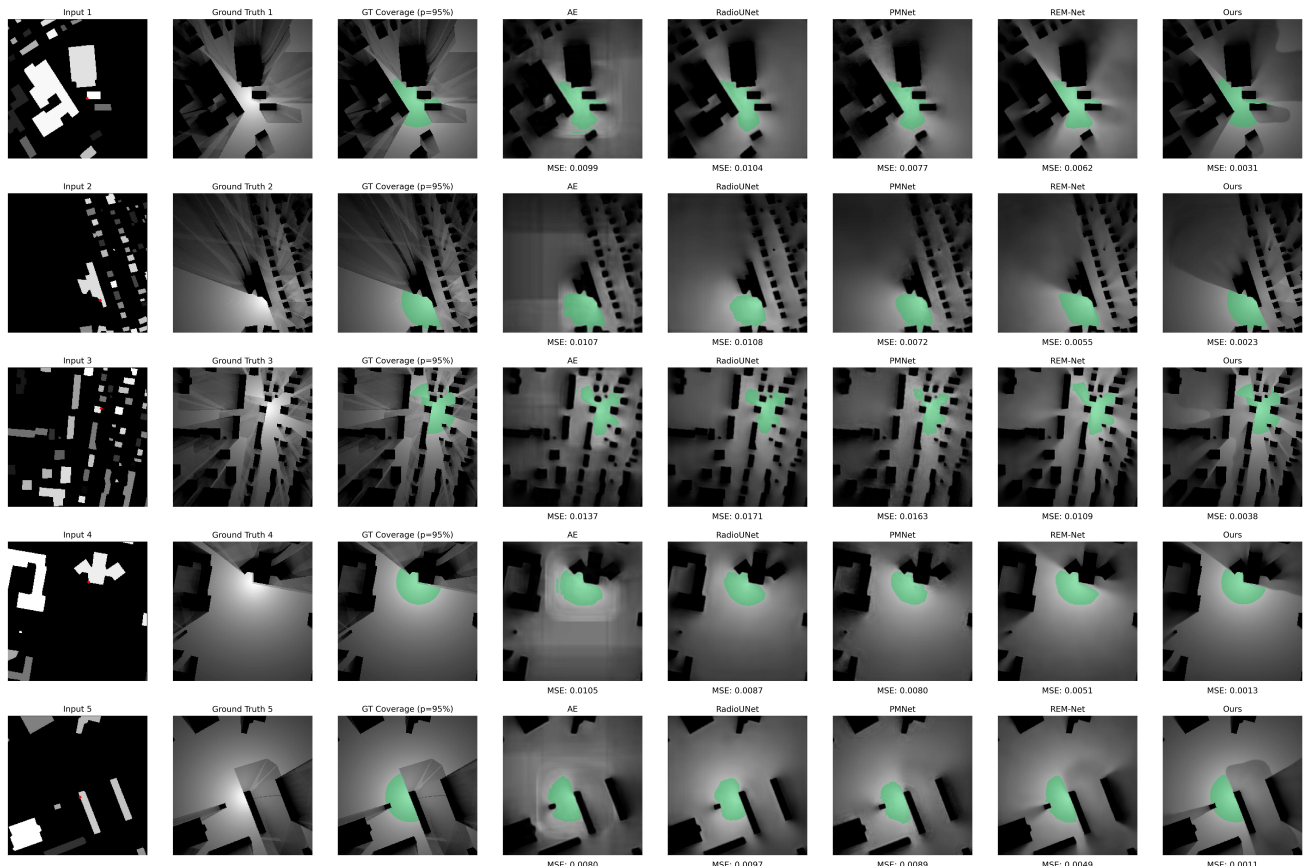


Fig. A14: Visualization cases of different models when dealing with the most important 5% of the coverage area.